# Determination of an Optimal Pharmacokinetic Model of $^{18}$F-FET for Quantitative Applications in Rat Brain Tumors

Marie Anne Richard, Jérémie P. Fouquet, Réjean Lebel, and Martin Lepage

*Centre d'imagerie moléculaire de Sherbrooke, Département de médecine nucléaire et radiobiologie, Université de Sherbrooke, Sherbrooke, Québec, Canada*

*O*-(2-$^{18}$F-fluoroethyl)-L-tyrosine ($^{18}$F-FET) is a radiolabeled artificial amino acid used in PET for tumor delineation and grading. The present study compares different kinetic models to determine which are more appropriate for $^{18}$F-FET in rats. **Methods:** Rats were implanted with F98 glioblastoma cells in the right hemisphere and scanned 9–15 d later. PET data were acquired during 50 min after a 1-min bolus of $^{18}$F-FET. Arterial blood samples were drawn for arterial input function determination. Two compartmental pharmacokinetic models were tested: the 2-tissue model and the 1-tissue model. Their performance at fitting concentration curves from regions of interest was evaluated using the Akaike information criterion, *F* test, and residual plots. Graphical models were assessed qualitatively. **Results:** Metrics indicated that the 2-tissue model was superior to the 1-tissue model for the current dataset. The 2-tissue model allowed adequate decoupling of $^{18}$F-FET perfusion and internalization by cells in the different regions of interest. Of the 2 graphical models tested, the Patlak plot provided adequate results for the tumor and brain, whereas the Logan plot was appropriate for muscles. **Conclusion:** The 2-tissue-compartment model is appropriate to quantify the perfusion and internalization of $^{18}$F-FET by cells in various tissues of the rat, whereas graphical models provide a global measure of uptake.

**Key Words:** FET; glioma; pharmacokinetic model

**J Nucl Med 2017; 58:1278–1284**
DOI: 10.2967/jnumed.116.180612

The radiolabeled artificial amino acid *O*-(2-$^{18}$F-fluoroethyl)-L-tyrosine ($^{18}$F-FET) has proven useful for the PET assessment of brain tumors in preclinical and clinical settings (*1–3*). Its high uptake in tumor tissue compared with normal brain and inflamed tissues allows for efficient tumor delineation (*4*), but the typical SUVs and tumor-to-brain ratios are of limited use for tumor grading (*5,6*). In contrast, the shape of time–activity curves are indicative of tumor grade and aggressiveness (*7*). For example, in untreated or recurring gliomas, continuously ascending curves are associated with a better prognosis than curves that reach a maximum a few minutes after injection (*6,8*), but the underlying mechanisms remain to be clarified (*7,9,10*). A pharmacokinetic model could help explain these differences and would allow quantitative comparison of cohorts.

Received Jul. 5, 2016; revision accepted Mar. 16, 2017.
For correspondence or reprints contact: Martin Lepage, Université de Sherbrooke, 3001 12th Ave. North, Sherbrooke, Québec, Canada, J1H 5N4.
E-mail: martin.lepage@usherbrooke.ca
Published online Mar. 30, 2017.


There have been few reports on $^{18}$F-FET pharmacokinetic modeling (*11,12*), and a consensus on the most appropriate models has not been proposed. The present study aims at identifying the best models in different tissue types.

## MATERIALS AND METHODS

### Animal Model

Experiments were conducted in accordance with the recommendations of the Canadian Council on Animal Care and the local Ethics Committee. F98 glioblastoma cells were implanted in the right hemisphere of 17 male Fischer rats (254.6 ± 15.9 g, Charles River Laboratories) according to a previously published protocol (*13*). The animals underwent dynamic PET scans 9–15 d after implantation. All imaging procedures were performed under isoflurane anesthesia with breathing rate and temperature continuously monitored. An automatic injector was used to administer the $^{18}$F-FET solution through a catheter in the caudal vein. Another catheter was inserted either in the caudal artery ($n = 10$) or in the femoral artery ($n = 7$) and used for manual blood sampling during the PET scan.

### Imaging Procedures

MRI was performed with a 7T small-animal scanner (Varian). The animals were subsequently transferred to a LabPET4 small-animal PET scanner (Gamma-Medica/GE Healthcare). Data were acquired in list mode over 50.5 min, with $^{18}$F-FET (26 ± 6 MBq) and Gd-DTPA (142.9 mM) coinjection of 500 μL (accounting for the catheter dead volume of 100 μL) performed at a rate of 400 μL/min at 0.5 min.

### Arterial Input Function (AIF) Determination

Blood sampling and tracer dosing were performed according to a published protocol (*14*). The plasma curve (Fig. 1A) was fitted to the following biexponential model (*15*) using least-squares fitting in MATLAB (The MathWorks):

$$C_p(t) = A \times \prod_{t_f}^{t_i}(t) \otimes \left( w_d e^{-\frac{t}{t_d}} + w_e e^{-\frac{t}{t_e}} \right), \qquad \text{Eq. 1}$$

where $A$ is the injection rate (% of injected dose/min), $\prod_{t_f}^{t_i}(t)$ is the boxcar function with amplitude 1 between the start and end of the injection, and $\otimes$ is the convolution operator. Distribution and elimination are modeled as decreasing exponential functions with characteristic times, $t_d$ and $t_e$ (min), and characteristic weights, $w_d$ and $w_e$ ($mL^{-1}$). The Gd-DTPA AIF was also measured but was used for the purpose of another study.

### Image Processing and Modeling

PET images were reconstructed using a maximum likelihood expectation maximization algorithm and 15 iterations. Random coincidences, scatter, decay, and attenuation corrections were part of the

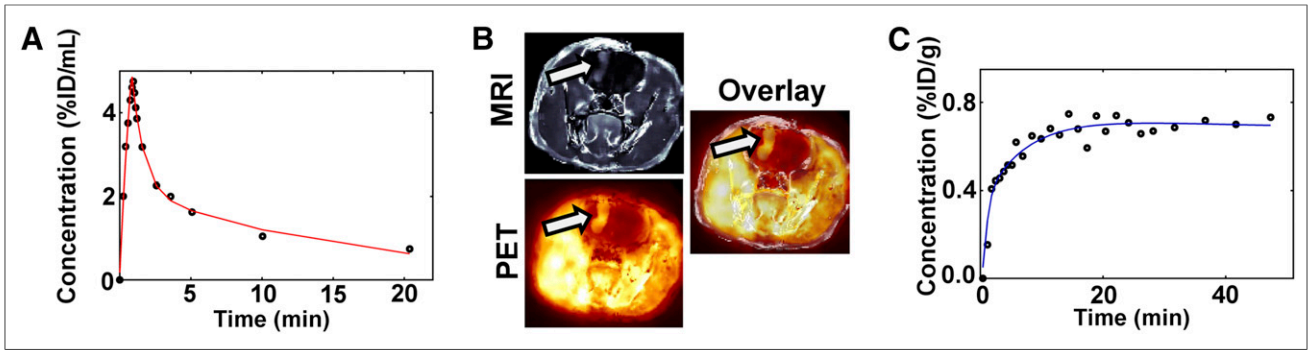


**FIGURE 1.** Pharmacokinetic modeling of $^{18}$F-FET in rat glioma model. (A) Experimental blood concentration curve and fitted AIF model. (B) Registered PET and MR images (tumor is indicated by arrow). (C) Time–activity curve for tumor ROI and representative fit of 2-tissue model.

reconstruction process. Different frame durations were tested (Supplemental Fig. 1; supplemental materials are available at http://jnm.snmjournals.org), and data are presented for the following time intervals: 1 × 50 s, 8 × 40 s, 10 × 1.5 min, 4 × 2 min, 3 × 5 min, and 1 × 6.3 min. PET images were converted to percentage injected dose per gram of tissue and registered, using ANTs (Penn Image Computing and Science Laboratory), to the MR images (Fig. 1B). Similar-sized regions of interest (ROIs) were drawn manually on the MR images over the tumor, the contralateral brain hemisphere, and the right temporal muscle and copied onto the registered PET images. Time–activity curves were extracted, and modeling was performed in MATLAB using uniformly weighted, trust-region-reflective least-squares fitting (Fig. 1C). Weighting based on the variance of data in each frame was also examined (Supplemental Fig. 2).

### Model Selection

Pharmacokinetic models have been extensively studied and applied to several other radiolabeled amino acids (*16,17*). Similarities between the transport mechanisms of these radiotracers (*18,19*) provide a starting point to determine a suitable $^{18}$F-FET model. However, unlike certain tracers, $^{18}$F-FET is known to produce only a few metabolites that are quickly eliminated from the blood pool (*4*). Also, contrary to its natural counterpart, $^{18}$F-FET is not incorporated into proteins (*4,20*).

Two classic compartment models will be tested: the 2-tissue model and the 1-tissue model (Fig. 2B). It is assumed that the voxels are sufficiently large such that diffusion of $^{18}$F-FET between voxels is negligible (*15*).

The differential equation describing the 1-tissue model is as follows:

$$\frac{dC_1}{dt} = K_1C_p - k_2C_1. \quad \text{Eq. 2}$$

The 2-tissue model is described by similar equations:

$$\begin{aligned}\frac{dC_1}{dt} &= K_1C_p - (k_2 + k_3)C_1 + k_4C_2 \\ \frac{dC_2}{dt} &= k_3C_1 - k_4C_2\end{aligned}, \quad \text{Eq. 3}$$

where $C_1$, $C_2$, and $C_p$ are the concentrations of $^{18}$F-FET in the first, second, and plasma compartment, respectively. For the 1-tissue model, the time–activity curve corresponds to $C_1$, and for the 2-tissue model, it corresponds to $C_1 + C_2$ (if the radioactivity from blood vessels within the tissue is negligible). For both models, $C_p$ represents the AIF. The kinetic parameters derived from the model are $K_1$ (mL/g/min), referred to as the flow constant, and $k_2$–$k_4$ (min$^{-1}$), the rate constants. Figure 2A outlines the significant steps in $^{18}$F-FET uptake. The 2-tissue model applies if there are 2 rate-limiting steps; otherwise, if there is a single rate-limiting step (i.e., when $k_3$ and $k_4$ are much faster than $K_1$ and $k_2$), the 1-tissue model applies. These steps can be any single process (e.g., $K_1$ represents the transport across the blood–brain barrier and $k_3$ the transport across the cell membrane)

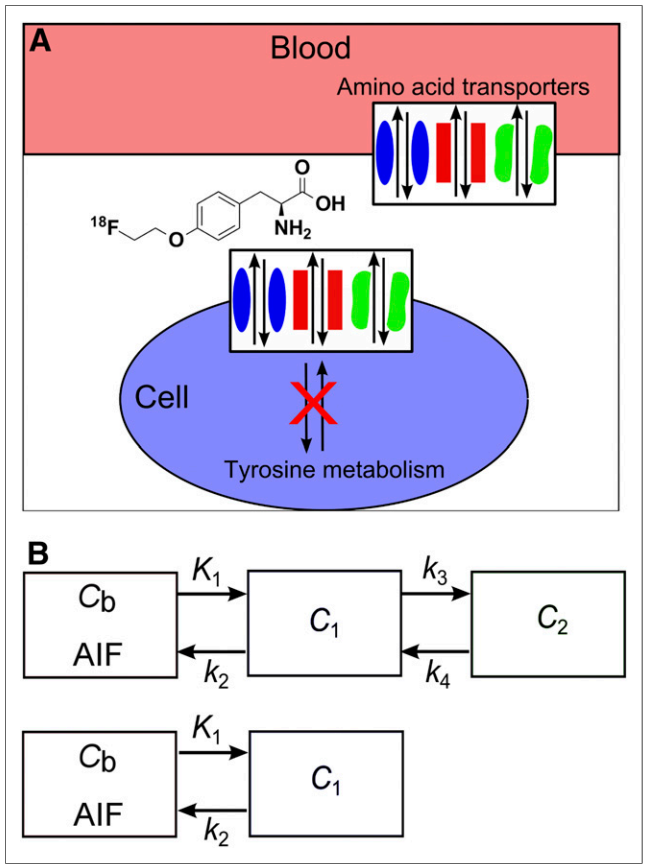


**FIGURE 2.** $^{18}$F-FET transport and kinetic models. (A) L-tyrosine and $^{18}$F-FET can cross capillary walls through specific transporters. In the case of highly permeable vessels, such as tumor neovascularization, passive diffusion is also possible. A variety of transporters are known to carry L-tyrosine and $^{18}$F-FET into cells (depending on cell type). Contrary to L-tyrosine, $^{18}$F-FET is not metabolized. (B) Compartment models are represented as black boxes indicating rate-limiting steps. Tracer concentration in each well-mixed compartment is denoted by *C*, and ($K_1$–$k_4$) are the transfer rate constants.

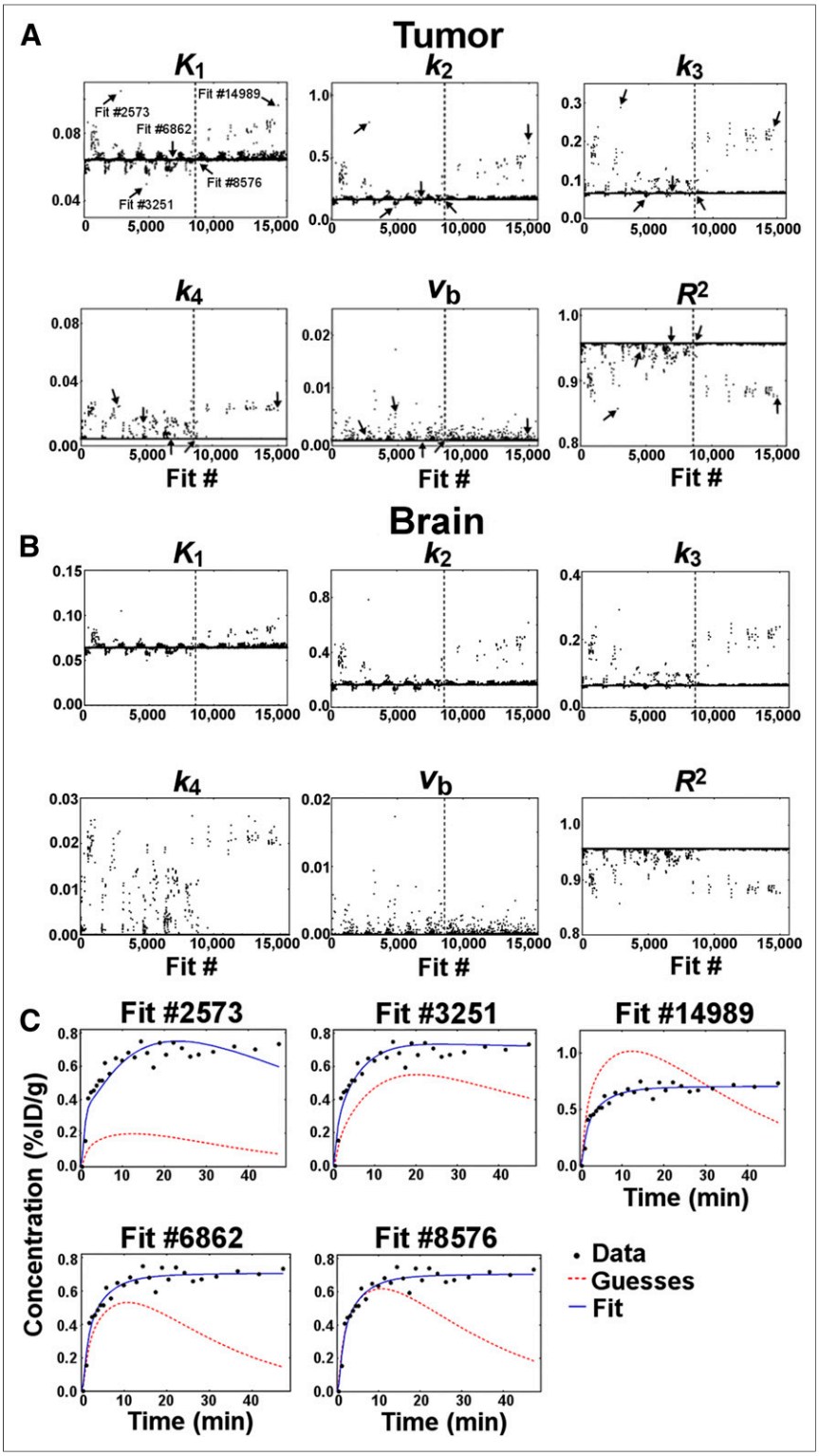


**FIGURE 3.** Effect of the initial parameter guesses on kinetic modeling for representative animal. (A and B) Effect of guess provided to fitting algorithm on resulting kinetic parameter values ($K_1$-$v_b$) and on fit quality ($R^2$). Each point represents value obtained with 1 of 15,680 sets of guesses. For example, x = 1 corresponds to the first set ($K_1 = 0.01$, $k_2 = 0.02$, $k_3 = 0.01$, $k_4 = 10^{-4}$, $v_b = 10^{-5}$), and x = 2 corresponds to the second set. Dashed vertical lines indicate guesses selected for remaining analyses. On graphs, points converging to most common value give impression of bold horizontal line. Arrows in A indicate results corresponding to different initial guesses illustrated in C. (C) Example of fits (solid line) for tumor. Dashed lines are initial curve provided to fitting algorithm. (Top) Fits with lower values of $R^2$. (Bottom) Fits with highest values of $R^2$.

or combined processes (e.g., $K_1$ represents the transport across the capillary wall and cell membrane).

Both models have similar solutions in the form of decreasing exponentials convolved with the AIF (*21*). Because the blood signal can contribute significantly to the time–activity curve, each model can include a blood volume fraction term, $v_b$ (adding $+ C_p v_b$ to the model). This term has been shown to improve kinetic models for highly perfused tissues (*22*). Models with and without a $v_b$ term will be compared.

Two graphical methods will also be tested: the Patlak method for irreversible uptake (*23*) and the Logan method for reversible uptake (*24*).

The Patlak plot is derived from the following equation:

$$\frac{C_t}{C_p} = K_i \frac{\int_0^t C_p(\tau)d\tau}{C_p} + V, \qquad \text{Eq. 4}$$

where $C_t$ is the time–activity curve, $K_i = \frac{K_1 k_3}{(k_2 + k_3)}$ is the influx rate, and $V$ is a combination of $v_b$ and the reversible compartment distribution volume (DV). Linearity in the Patlak plot indicates irreversible uptake over the scan period (*23,25*).

The Logan plot is defined as follows:

$$\frac{\int_0^t C_t(\tau)d\tau}{C_t} = DV \frac{\int_0^t C_p(\tau)d\tau}{C_t} + int, \qquad \text{Eq. 5}$$

where $DV = \frac{K_1}{k_2} + v_b$ is the distribution volume for the 1-tissue model, which becomes $DV = \frac{K_1}{k_2}\left(1 + \frac{k_3}{k_4} + v_b\right)$ for the 2-tissue model; and int is the intercept. All these values are explained in detail by Logan (*24*).

### Compartment Model Quality Metrics

Compartment models are based on nonlinear equations that must be solved iteratively. This poses a few problems, notably: (1) initial parameter guesses can significantly affect results, and (2) the coefficient of determination ($R^2$) is not the best metric to compare nonlinear models. Notably, it has been shown through simulations that a better model can have an identical or lower $R^2$ than a poorer model (*26*).

To solve issue 1, the best fit for each model was determined from a wide range of initial guesses. A first set of guesses was based on the initial slope and the washout pattern, and then each parameter was varied over ±100% of the original value. The optimal set of guesses was selected on the basis of $R^2$, which is adequate to compare the results of a single model. The sensitivity of the kinetic parameters to the initial guesses (fit

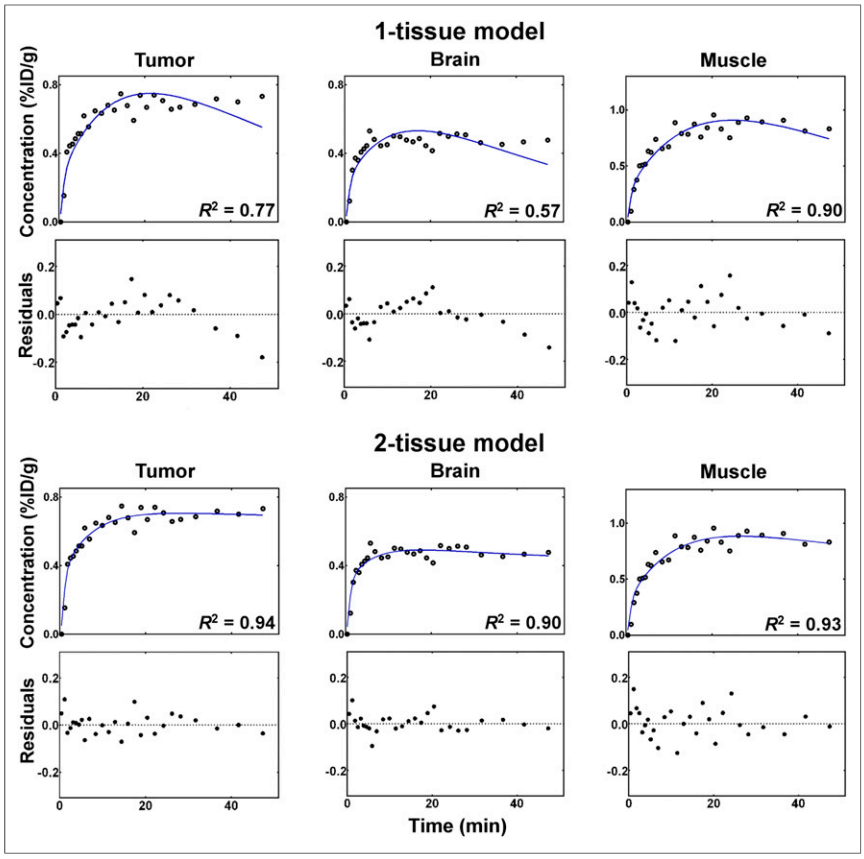


**FIGURE 4.** Compartment model fits for representative animal. Best fits of time–activity curves with 1-tissue and 2-tissue models. Residuals are shown below their respective fits.

stability) was evaluated at the same time. This was performed for all animals.

To solve issue 2, best fits were compared based on 2 quantitative criteria validated for nonlinear models (*27*). These criteria penalize the addition of superfluous parameters (i.e., overfitting).

The first criterion is the $F$ test comparing 2 models (models 1 and 2):

$$F = \frac{(\mathrm{RSS}_1 - \mathrm{RSS}_2)/(\mathrm{df}_1 - \mathrm{df}_2)}{\mathrm{RSS}_2/\mathrm{df}_2}, \qquad \text{Eq. 6}$$

where RSS is the residual sum of squares, and df is the degrees of freedom (number of data points minus the number of fitted parameters).

**TABLE 1**
*F* Test *P* Values Comparing Compartment Models Based on Population Average

| Model | Tumor | Muscle | Brain |
|---|---|---|---|
| 2-tissue model vs. 1-tissue model | <0.0001 | <0.0001 | <0.0001 |
| Reversible vs. irreversible 2-tissue model | >0.05 | >0.05 | >0.05 |

Reversible (fitted $k_4$), irreversible ($k_4 = 0$). A $P$ value of ≤ 0.05 indicates that the model with more parameters yielded a better fit to the data.

The $F$ statistics is used to extract a $P$ value. If the $P$ value is 0.05 or less, the model with more parameters (model 2) is considered a better fit.

The second criterion is the Akaike information criterion (AIC) (*28*) modified for small samples (AICc, $n/k < 40$):

$$\mathrm{AICc} = n\ln\frac{\mathrm{RSS}}{n} + 2k + 2k(k+1)/(n-k-1), \qquad \text{Eq. 7}$$

where $n$ is the sample size, and $k$ is the number of fitted parameters. The best model minimizes the AICc.

Note that a population-average RSS was used to compute both the $F$ value and AICc. Uncertainties were derived from the SD of the RSS distribution.

In addition to these metrics, the residual plots were analyzed, and interanimal variability was assessed by computing the coefficient of variation (COV) (%):

$$\mathrm{COV} = \frac{\sigma}{\mu}, \qquad \text{Eq. 8}$$

where σ is the SD of the kinetic parameter in the cohort and μ its mean value.

Finally, the parameters derived from each model were examined to see whether differences were observed between tissues.

## RESULTS

### Fit Stability

The 2-tissue model is sensitive to initial guesses when all parameters are free to vary. A nested loop algorithm was used to test multiple initial guesses sets. The kinetic parameters resulting from these trials were plotted as a function of the trial number (Fig. 3). For example, the first point on the graph, titled $K_1$, represents the values of $K_1$ for trial 1. This was repeated for the tumor (Fig. 3A), brain (Fig. 3B), and muscle (Supplemental Fig. 3). More than 90% of fits returned the same parameter values (within a 1% error margin) and had high $R^2$. Because of the wide range of initial guesses tested, the existence of a better solution is improbable. For the other 10% of fits, the algorithm stopped before reaching a better solution because the variation in the sum of squares was less than the threshold ($10^{-8}$), which is indicative of a local minimum. Inspection of the initial curves provided to the fitting algorithm (Fig. 3C) suggests that local minima are encountered when the initial uptake slope and maximum concentration are poorly estimated. This phenomenon is most important for very low (0.01 mL/g/min) and very high (0.1 mL/g/min) values of $K_1$, the main parameter modulating initial uptake. Cyclic variations in other parameters (especially high values of $k_4$ and $v_b$) are responsible for smaller deviations. Because $v_b$ and $k_4$ fitted for the tumor and brain are consistently small, it is possible to set these to zero. In this case, the model always converges to the best solution. In muscles, $k_4$ is nonzero, so this method cannot be used and only setting $v_b$ does not improve fit stability. In all cases, the same optimal set of guesses could be used for all animals and ROIs.

**TABLE 2**
AIC for Different Compartment Models Based on Population Average

| Model | Tumor | Muscle | Brain |
|---|---|---|---|
| 2TM + $v_b$ | 68 ± 21 | 123 ± 38 | 63 ± 33 |
| 2TM | 67 ± 20* | 122 ± 38* | 62 ± 33 |
| Irreversible 2TM + $v_b$ | 67 ± 20* | 123 ± 38 | 62 ± 31 |
| Irreversible 2TM | 67 ± 19* | 123 ± 38 | 61 ± 29* |
| 1TM + $v_b$ | 141 ± 29 | 138 ± 33 | 130 ± 33 |
| 1TM | 148 ± 33 | 138 ± 32 | 136 ± 33 |

*Lowest values (smallest AICc).
2TM = 2-tissue model; +$v_b$ = including contribution of the blood volume fraction; 1TM = 1-tissue model; Irreversible ($k_4$ = 0). Data are mean ± SD.

**TABLE 3**
COV (%) for Different Models

| Model | Tumor | Muscle | Brain |
|---|---|---|---|
| COV $K_1$ | | | |
| 2TM + $v_b$ | 24.30* | 39.90 | 28.06* |
| Irreversible 2TM | 26.91 | 30.13* | 31.01 |
| 1TM + $v_b$ | 34.06 | 37.69 | 34.71 |
| COV $k_2$ | | | |
| 2TM + $v_b$ | 61.58 | 51.72 | 51.57 |
| Irreversible 2TM | 61.98 | 48.32* | 46.15 |
| 1TM + $v_b$ | 40.31* | 49.64 | 40.58* |
| COV $k_3$ | | | |
| 2TM + $v_b$ | 39.10 | 52.22* | 25.20* |
| Irreversible 2TM | 31.93* | 64.88 | 31.16 |
| COV $k_4$ | | | |
| 2TM + $v_b$ | Not applicable† | 159 | Not applicable† |
| COV $K_i$ | | | |
| Patlak | 27.10 | 25.52 | 25.39 |
| COV DV | | | |
| Logan | 39.39 | 36.62 | 41.31 |

*Lowest values.
†Not applicable because values are close to zero ($<10^{-5}$).
2TM = 2-tissue model; +$v_b$ = including contribution of the blood volume fraction; 1TM =1-tissue model.
Irreversible ($k_4$ = 0). Note that $v_b$ is almost zero for all ROIs.

Finally, the 1-tissue model is stable with regards to initial guesses (Supplemental Fig. 4).

### Fit Quality

Visual inspection of the fitted curves indicates that the 2-tissue model fits the experimental data more closely than the 1-tissue model (Fig. 4). The *F* test (Table 1) further confirms that the 2-tissue model is superior to the 1-tissue model; however, it does not establish superiority of the reversible 2-tissue model ($k_4$ is fitted) over its irreversible counterpart ($k_4$ = 0). Additional comparisons between model variants were performed using the AICc. The irreversible 2-tissue model without $v_b$ minimized the AICc for the brain, whereas the reversible 2-tissue model without $v_b$ proved superior for muscles (Table 2). Results are inconclusive for the tumor, and there is a large uncertainty on the AICc for all ROIs. Therefore, it is impossible to base the choice of model on this criterion only.

The previous metrics are useful to compare models, but not to identify their weaknesses. Random distribution of the residuals (Fig. 4) would be expected to reflect the normal distribution of experimental data. Any pattern warrants explanation and adjustment of the model. For example, the residual plot for the 1-tissue model shows a distinctive inverted U shape that is most obvious for the tumor and brain. This shape is observed when a model has too few degrees of freedom to properly fit the data, yielding over- and undershooting.

### Graphical Analysis

The Patlak plots (Fig. 5A) are linear in the latter portion of the curve ($t \geq 20$ min) for the tumor and brain. For muscles, there is a slight deviation, which may be associated with reversible uptake. The opposite is observed for Logan plots (Fig. 5B) where linearity is reached rapidly ($t \geq 10$ min) in muscles, whereas such linearity is reached much later, if at all, in the tumor and brain. This delay suggests that the tracer is trapped in the tumor and brain over the scan period.

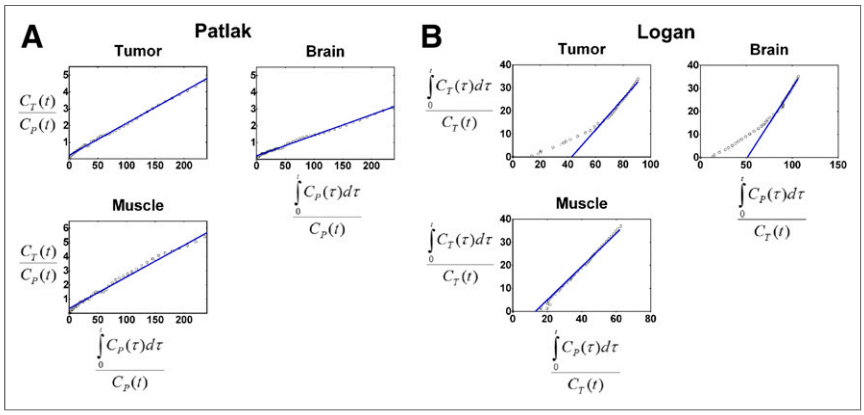


**FIGURE 5.** Patlak (A) and Logan (B) plots for representative animal. Slope (straight blue lines) is obtained by fitting linear region in last part of plot.

### Interanimal Variability

The COV was calculated for kinetic parameters of the 1- and 2-tissue models, as well as for $K_i$ of the Patlak plot and DV of the Logan plot (Table 3). No compartment model is clearly superior in terms of decreased variability, and COV for graphical models tends to be smaller than for the compartment models. Overall, the Patlak $K_i$ has the smallest COV.

### Kinetic Parameters

The SE on kinetic parameters was derived from the residuals and covariance matrix. It is under 5% for all parameters of the 1-tissue model. For the 2-tissue model, it

is under 10% for $K_1$, under 20% for $k_2$ and $k_3$, and over 200% for $k_4$ and $v_b$. Setting $k_4$ and $v_b$ to zero for the tumor and brain results in a SE under 5% for the remaining parameters.

Parameter differences between ROIs were assessed using paired and unpaired *t* tests with control for false discovery rate (Fig. 6 and Supplemental Fig. 5, respectively). For the 2-tissue model, muscles have significantly lower $k_2$ and $k_3$ than both the brain and the tumor, whereas the tumor has significantly higher $k_3$ than the other ROIs. Values of $k_4$ and $v_b$ are small and highly variable for all ROIs and show no significant differences. For the 1-tissue model, both $K_1$ and $k_2$ are highest in muscles, and the tumor has a higher $K_1$ and a lower $k_2$ than the brain. Values of $v_b$ are much higher and less variable than for the 2-tissue model. Finally, for the graphical models, both $K_i$ and DV are highest in muscles, followed by the tumor, with the brain having the lowest values. $K_i$ could also be calculated from the 2-tissue model parameters. There are no significant differences between the $K_i$ obtained with either method. DV could not be calculated from the 2-tissue model for the brain and tumor because $k_4$ is close to zero. For muscles, it proves more variable than the Logan DV due to variability in $k_4$ estimations. Supplemental Figure 6 shows parameter maps for the tumor of a representative animal.

## DISCUSSION

### Model Choice

The AICc and *F* test establish the superiority of the 2-tissue-compartment model over the 1-tissue model. The small differences and large SD for the AICc do not allow us to draw firm conclusions about variants of the 2-tissue model. However, the AICc and the graphical analysis agree for the brain (irreversible uptake) and muscle (slight reversibility). For the tumor, graphical analysis indicates that the irreversible Patlak model applies and that the Patlak $K_i$ agrees with the $K_i$ results from the 2-tissue model. According to unpublished analyses, scan duration significantly affects graphical analysis results such that reversibility should be assessed for other experimental conditions. Finally, parameters derived from graphical analysis have lower interanimal variability, which makes statistical comparisons of cohorts easier. However, they cannot distinguish between perfusion and internalization by cells.

### Model Variants and Limitations

Different 2-tissue model variants are possible. Some take into account the contribution of blood to the signal ($v_b$) or release of $^{18}$F-FET by cells ($k_4$). Setting $v_b$ or $k_4$ to zero may improve fit stability but should be justified by the underlying biology or experimental limitations. The low and highly variable $v_b$ observed in the present study is attributed to a lack of information on the first-pass bolus (i.e., absence of a sharp initial time–activity curve peak) due to insufficient time resolution or low perfusion in the rat. The need to include $k_4$ depends on tissue type. For example, $^{18}$F-FET appears trapped in the brain and tumor during the scan period. This result, consistent with an early study of $^{18}$F-FET uptake in gliomas (*29*), justifies setting $k_4$ to zero. In contrast, for muscles, $^{18}$F-FET internalization may be reversible such that including $k_4$ was deemed preferable, even though it is small and highly variable between animals (Table 3). Because different tumors use different $^{18}$F-FET uptake mechanisms (*4*), these results apply to the F98 glioblastoma, but tumors with similar energy-independent $^{18}$F-FET uptake mechanisms, such as human gliomas (*30*), are likely to show similar kinetics, although $v_b$ is expected to be significant in humans.

In this study, graphical analysis proved the best tool to assess reversibility, whereas interanimal variability and curve shape justified neglecting $v_b$. However, probabilistic algorithms that select the optimal model could facilitate $^{18}$F-FET modeling (*31*).

Finally, radiometabolites were not measured in this study. The fraction of $^{18}$F-FET metabolites in humans was provided by Langen et al. (*4*). We did not assume it to be similar in rats and did not correct the AIF—this is a limitation of our study.

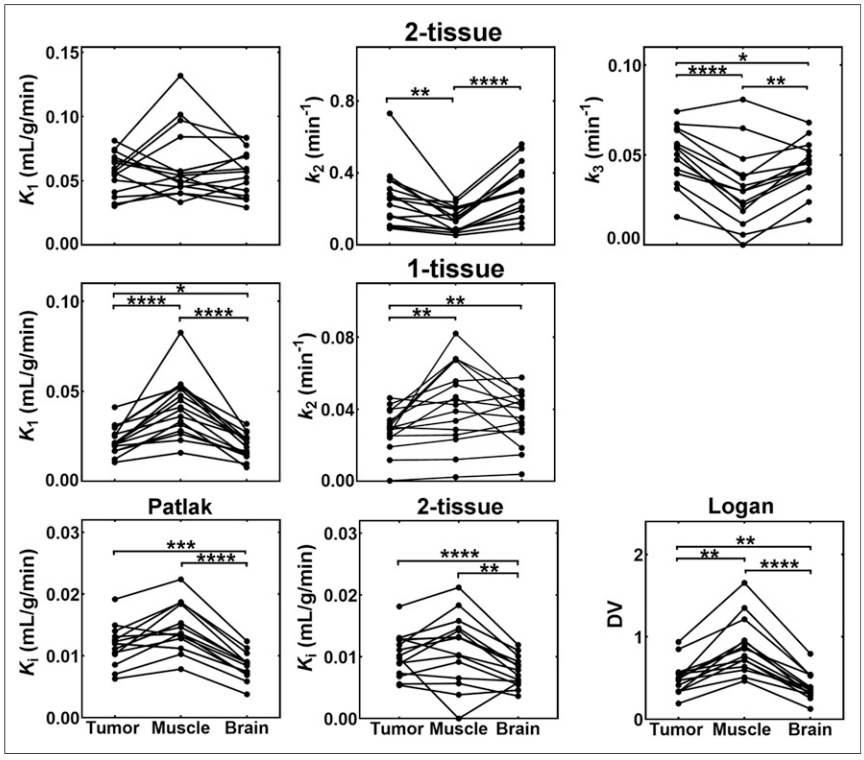


**FIGURE 6.** Results of pharmacokinetic modeling. Kinetic parameters for each animal derived by compartmental and graphical methods ($n$ = 16 for both, 1 animal had no visible tumor and was excluded). Outliers were removed in GraphPad Prism (ROUT $Q$ = 1%) for analysis but are shown here. *$P \leq 0.05$, **$P \leq 0.01$, ***$P \leq 0.001$, ****$P \leq 0.0001$, false discovery rate–controlled.

### Comparison of Kinetic Parameters Between Models

Late image frames (Fig. 1B) show the highest concentration of $^{18}$F-FET in muscles, followed by the tumor, with little uptake in the brain. This is reflected in the values of $K_i$ and DV, as well as in a higher $K_1$ for the 1-tissue model. However, the 2-tissue model suggests different uptake

mechanisms for muscles and the tumor. In this case, all tissues have similar values of $K_1$, but $k_2$ and $k_3$ are generally lower for muscles than for the tumor or brain, indicating that $^{18}$F-FET tends to remain in the reversible compartment (most likely the extracellular–extravascular space (*30*)). On the other hand, values of $k_3$ are highest in the tumor, suggesting that the principal accumulation mechanism of $^{18}$F-FET in F98 glioblastoma is internalization. Finally, the low signal in the brain arises from a combination of slower uptake and similar washout compared with the tumor. This is an example of how modeling can decouple and quantify different physiologic processes.

## CONCLUSION

The 2-tissue-compartment model is appropriate for quantifying the perfusion and internalization of $^{18}$F-FET in the tumor, brain, and muscles of F98 brain tumor–bearing rats. The Patlak plot can evaluate uptake in the tumor or brain, whereas the Logan plot is preferable for muscles. However, verifying the impact of scan duration on reversibility before choosing between reversible and irreversible models is advised. In human gliomas, because of similar $^{18}$F-FET uptake mechanisms, the same models should apply, although the contribution of $v_b$ must be assessed. Validation in humans or other animals could easily be performed using the tools presented here.

## DISCLOSURE

This project was funded through NSERC grant RGPIN-2014-05386. Marie Anne Richard is supported by scholarships from the NSERC (CGS M) and FRQNT (B1). Martin Lepage is a member of the FRQS-funded CRCHUS. No other potential conflict of interest relevant to this article was reported.

## REFERENCES

1. Lee TS, Ahn SH, Moon BS, et al. Comparison of $^{18}$F-FDG, $^{18}$F-FET and $^{18}$F-FLT for differentiation between tumor and inflammation in rats. *Nucl Med Biol.* 2009;36:681–686.
2. Wang HE, Wu SY, Chang CW, et al. Evaluation of F-18-labeled amino acid derivatives and [$^{18}$F]FDG as PET probes in a brain tumor-bearing animal model. *Nucl Med Biol.* 2005;32:367–375.
3. Galldiks N, Langen KJ, Pope WB. From the clinician's point of view: what is the status quo of positron emission tomography in patients with brain tumors? *Neuro-oncol.* 2015;17:1434–1444.
4. Langen KJ, Hamacher K, Weckesser M, et al. O-(2-[$^{18}$F]fluoroethyl)-l-tyrosine: uptake mechanisms and clinical applications. *Nucl Med Biol.* 2006;33:287–294.
5. Pöpperl G, Kreth FW, Herms J, et al. Analysis of $^{18}$F-FET PET for grading of recurrent gliomas: is evaluation of uptake kinetics superior to standard methods? *J Nucl Med.* 2006;47:393–403.
6. Pöpperl G, Kreth FW, Mehrkens JH, et al. FET PET for the evaluation of untreated gliomas: correlation of FET uptake and uptake kinetics with tumour grading. *Eur J Nucl Med Mol Imaging.* 2007;34:1933–1942.
7. Weckesser M, Langen KJ, Rickert CH, et al. O-(2-[$^{18}$F]fluorethyl)-L-tyrosine PET in the clinical evaluation of primary brain tumours. *Eur J Nucl Med Mol Imaging.* 2005;32:422–429.
8. Niyazi M, Jansen N, Ganswindt U, et al. Re-irradiation in recurrent malignant glioma: prognostic value of [$^{18}$F]FET-PET. *J Neurooncol.* 2012;110:389–395.
9. Zhang K, Langen K, Neuner I, et al. Relationship of regional cerebral blood flow and kinetic behaviour of O-(2-$^{18}$F-fluoroethyl)-L-tyrosine uptake in cerebral gliomas. *Nucl Med Commun.* 2014;35:245–251.
10. Miyagawa T, Oku T, Uehara H, et al. "Facilitated" amino acid transport is upregulated in brain tumors. *J Cereb Blood Flow Metab.* 1998;18:500–509.
11. Kratochwil C, Combs SE, Leotta K, et al. Intra-individual comparison of $^{18}$F-FET and $^{18}$F-DOPA in PET imaging of recurrent brain tumors. *Neuro-oncol.* 2014;16:434–440.
12. Thiele F, Ehmer J, Piroth MD, et al. The quantification of dynamic FET PET imaging and correlation with the clinical outcome in patients with glioblastoma. *Phys Med Biol.* 2009;54:5525–5539.
13. Mathieu D, Lecomte R, Tsanaclis AM, Larouche A, Fortin D. Standardization and detailed characterization of the syngeneic Fischer/F98 glioma model. *Can J Neurol Sci.* 2007;34:296–306.
14. Poulin É, Lebel R, Croteau E, et al. Conversion of arterial input functions for dual pharmacokinetic modeling using Gd-DTPA/MRI and $^{18}$F-FDG/PET. *Magn Reson Med.* 2013;69:781–792.
15. Pellerin M, Yankeelov TE, Lepage M. Incorporating contrast agent diffusion into the analysis of DCE-MRI data. *Magn Reson Med.* 2007;58:1124–1134.
16. Wardak M, Schiepers C, Cloughesy TF, Dahlbom M, Phelps ME, Huang SC. $^{18}$F-FLT and $^{18}$F-FDOPA PET kinetics in recurrent brain tumors. *Eur J Nucl Med Mol Imaging.* 2014;41:1199–1209.
17. Wiesel FA, Halidin C, Sjogren I, Bjerkenstedt L. The transport of tyrosine into the human brain as determined with L-[1-$^{11}$C] tyrosine and PET. *J Nucl Med.* 1991;32:2043–2049.
18. Juhász C, Dwivedi S, Kamson DO, Michelhaugh SK, Mittal S. Comparison of amino acid positron emission tomographic radiotracers for molecular imaging of primary and metastatic brain tumors. *Mol Imaging.* 2014;13:5218–5225.
19. Jager PL, Vaalburg W, Pruim J, de Vries EG, Langen KJ, Piers DA. Radiolabeled amino acids: basic aspects and clinical applications in oncology. *J Nucl Med.* 2001;42:432–445.
20. Heiss P, Mayer S, Herz M, Wester HJ, Schwaiger M, Senekowitsch-Schmidtke R. Investigation of transport mechanism and uptake kinetics of O-(2-[$^{18}$F]fluoroethyl)-L-tyrosine in vitro and in vivo. *J Nucl Med.* 1999;40:1367–1373.
21. Phelps ME, Huang SC, Hoffman EJ, Selin C. Tomographic measurement of local cerebral glucose metabolic rate in humans with validation of method. *Ann Neurol.* 1979;6:371–388.
22. Sourbron SP, Buckley DL. On the scope and interpretation of the Tofts models for DCE-MRI. *Magn Reson Med.* 2011;66:735–745.
23. Patlak CS, Blasberg RG, Fenstermacher JD. Graphical evaluation of blood-to-brain transfer constants from multiple-time uptake data. *J Cereb Blood Flow Metab.* 1983;3:1–7.
24. Logan J. Graphical analysis of PET data applied to reversible and irreversible tracers. *Nucl Med Biol.* 2000;27:661–670.
25. Gambhir SS, Schwaiger M, Huang SC, et al. Simple noninvasive quantification method for measuring myocardial glucose utilization in humans employing positron emission tomography and fluorine-18 deoxyglucose. *J Nucl Med.* 1989;30:359–366.
26. Spiess AN, Neumeyer N. An evaluation of $R^2$ as an inadequate measure for nonlinear models in pharmacological and biochemical research: a Monte Carlo approach. *BMC Pharmacol.* 2010;10:6.
27. Glatting G, Kletting P, Reske SN, Hohl K, Ring C. Choosing the optimal fit function: comparison of the Akaike information criterion and the F-test. *Med Phys.* 2007;34:4285–4292.
28. Akaike H. A new look at the statistical model identification. *IEEE Trans Automat Contr.* 1974;19:716–723.
29. Wester HJ, Herz M, Weber W, et al. Synthesis and radiopharmacology of O-(2-[$^{18}$F]fluoroethyl)-L-tyrosine for tumor imaging. *J Nucl Med.* 1999;40:205–212.
30. Habermeier A, Graf J, Sandhöfer BF, Boissel JP, Roesch F, Closs EI. System l amino acid transporter LAT1 accumulates O-(2-fluoroethyl)-l-tyrosine (FET). *Amino Acids.* 2015;47:335–344.
31. Zhou Y, Aston JAD, Johansen AM. Bayesian model comparison for compartmental models with applications in positron emission tomography. *J Appl Stat.* 2013;40:993–1016.